HAL
open science

Modeling multilayer coating systems in solar receivers

Danying Chen, Alexandre Crisci, Raphaël Boichot, Johann Colas, Ludovic Charpentier, Marianne J.H. Balat-Pichelin, Michel Pons, Frédéric Mercier

To cite this version:

Danying Chen, Alexandre Crisci, Raphaël Boichot, Johann Colas, Ludovic Charpentier, et al.. Modeling multilayer coating systems in solar receivers. Surface and Coatings Technology, 2020, 399, pp.126102. 10.1016/j.surfcoat.2020.126102 . hal-02904030

HAL Id: hal-02904030

https://hal.science/hal-02904030v1

Submitted on 21 Jul 2020

HAL is a multi-disciplinary open access archive for the deposit and dissemination of scientific research documents, whether they are published or not. The documents may come from teaching and research institutions in France or abroad, or from public or private research centers.

L'archive ouverte pluridisciplinaire **HAL**, est destinée au dépôt et à la diffusion de documents scientifiques de niveau recherche, publiés ou non, émanant des établissements d'enseignement et de recherche français ou étrangers, des laboratoires publics ou privés.

Modeling multilayer coating systems for their application in solar receivers

Danying Chen[a], Alexandre Crisci[a], Raphaël Boichot[a], Johann Colas[b], Ludovic Charpentier[b], Marianne Balat-Pichelin[b], Michel Pons[a] and Frédéric Mercier[a,*]

[a] *Univ. Grenoble Alpes, CNRS, Grenoble INP, SIMAP, 38000 Grenoble, France*
[b] *PROMES-CNRS, 7 rue du Four Solaire, F-66120 Font-Romeu Odeillo, France*

ARTICLE INFO

Keywords:
Concentrated solar power plants
Multilayer coating
Oxidation
Creep relaxation
Stress evolution
Computer simulation

ABSTRACT

A comprehensive model to predict the stress evolution in a multilayer coating during its use in solar receivers is proposed. The model takes into account residual stress in the coatings, thermal gradient in the structure and high temperature phenomena like oxide scale growth and creep relaxation. The numerical tool developed in this work can help to understand the complex interplay of these phenomena occurring in all the materials involved. Additionally, the present model can be used to assess high temperature data like creep when it is compared with an experimental case.

1. Introduction

The central receiver system, one of the main concentrating solar power (CSP) technologies is now moving to the forefront and becoming an emerging option for large-scale electricity production. A CSP must demonstrate high longevity (>30 years) while operating in extreme conditions : high temperatures, cyclic oxidation quelle REF?. The periodic temperature changes and/or non-uniform temperature fields within the system during operation lead to the generation of thermal stresses in the system. Moreover, as the operation period extends, high temperature phenomena like creep deformation, oxidation as well as phase transformation take place, leading to the redistribution of stress field in the system. The question of which material is the most suitable for different temperatures is still under study quelle REF?.

Among the possible choices for the material of the receiver, multilayer coating systems appears as promising candidates. In such systems, delamination and/or failure of coatings occur when the stress in coatings approaches their critical strength, resulting in a loss of protection for the metallic substrate in high temperature environment. For this reason, ongoing researches focus on stress evolution in multilayer coating systems subjected to external (thermal and/or mechanical) loading(s) to fulfill the following objectives: 1) to understand the role of external loads and the influence of the aforementioned high temperature phenomena 2) to estimate and further improve the reliability and durability of the coating(s)/substrate systems for multilayer coating system in CSP technology.

To our knowledge, a comprehensive model that could fulfil these two objectives is lacking today. Although modeling of oxide growth scale on metallic substrate combined with creep deformation can be found in literature [1–7], a lot of characteristics of CSP solar receivers are not taken into account in the previous studies like 1) thermal gradient induced in the system by the solar radiation flux on the top surface and heat exchange with of an heat transfer fluid 2) coating on all surfaces of the receiver 3) impact of initial residual stress in the coating induced by the deposition technique. The purpose of this work is to provide a comprehensive model to predict the stress evolution of the system, including initial residual stress, thermal gradient, oxide scale growth and creep relaxation. After a description of the model, it is applied to a multilayer system composed of a molybdenum-based alloy coated with AlN polycristalline film. This part aims at understanding the complex links between the existing high temperature phenomena. In a second part, the model is applied and compared with an experimental case, an iron-based alloy coated with an AlN/Al_2O_3 multilayer subject to cyclic thermal oxidation. In that case, we show that the model can be used to assess high temperature data like the creep activation energy.

*Corresponding author
frederic.mercier@simap.grenoble-inp.fr (F. Mercier)
ORCID(s):

2. Experimental details

For the substrates, a slow creeping oxide dispersion strengthened FeCrAl (Kanthal APMT, Sandvik) and a molybdenum-based alloy (TZM, Goodfellow Metal, 99 wt% Mo, 0.5 wt% Ti, 0.1 wt% Zr and C) are chosen. The thickness of TZM and APMT is 1 and 3 mm, respectively. Prior to AlN deposition, APMT is oxidised at 1100°C during 25 h to form a 1.5 µm thick alumina layer. This thermally grown alumina layer acts as an accommodation layer to avoid cracking during AlN synthesis. 40-µm-thick AlN coatings are deposited on all faces of the pre-oxidised substrate by chemical vapor deposition. Details on deposition conditions are given in [8]. Briefly, in-situ produced $AlCl_3$ (from reaction between Al and Cl_2 at 800 K) reacts with NH_3 to form AlN at 1200°C. In-plane residual stress of AlN thin films were estimated at room temperature after deposition by using the $\sin^2\psi$ method.

Cyclic oxidation is performed in a laboratory furnace at 1100°C under air. The sample was then removed rapidly from the furnace and naturally cooled down. After each cycle, the evolution of stress with oxidation time is obtained by Raman spectroscopy and Photoluminescence piezospectroscopy (T64000 spectrometer, Horiba Jobin-Yvon) at room temperature to evaluate the magnitude of stress in AlN and Al_2O_3 respectively. The excitation source is an Ar^+ -laser with 514 nm wavelength. Its power is adjusted to prevent shift of frequency resulting from heating of samples. The bi-axial residual stress in AlN is determined with the shift of E_2 phonon frequency [9]. The residual stress in the thermally grown alumina is deduced from the shift of the R-lines, coming from the photoluminecence of chromium impurities [10, 11].

3. Model construction

3.1. Schematic representation

A typical, stress-free multilayer system with a substrate coated in both faces is schematically illustrated in Fig. 1. The n individual layers are stacked to the upper part of a substrate, while m layers are stacked to the lower part. Each interface is considered to be flat and the bonding between two adjacent layers is considered to be perfect. The z-axis coordinate is defined such as the mid-plane of the substrate is located at z=0. The subscript t and b denote the layers above (z>0) or below (z<0) the substrate respectively, as well as i the layer number ranging from 1 to n (or m). The t1 layer is in direct contact with the upper surface of substrate. The thickness of substrate, oxide, and individual coating layers are denoted as t_s, $t_{o,t}$ or $t_{o,b}$, and $t_{c,ti}$ or $t_{c,bi}$ depending on their z position, respectively. $t_{o,t}$ represents the thickness of the oxide grown on the top surface of the system whereas $t_{o,b}$ is that of the oxide on the bottom surface. The z coordinate of the interface between the coating layers i+1 and i is defined as $z_{c,ki}$ with the following relationship:

$$z_{c,ki} = sign(k) \cdot (\frac{t_s}{2} + \sum_{j=1}^{i} t_{c,kj})$$
$$sign(k) = \begin{cases} 1 & k = t \\ -1 & k = b \end{cases} \tag{1}$$

Moreover, the z coordinates at the outer-surface of the oxides are:

$$z_{o,t} = \frac{t_s}{2} + \sum_{i=1}^{n} t_{c,ti} + t_{o,t} \tag{2a}$$

$$z_{o,b} = -(\frac{t_s}{2} + \sum_{i=1}^{m} t_{c,bi} + t_{o,b}) \tag{2b}$$

Usually, the total thickness of a multilayer coating system is much smaller than its in-plane dimensions (x-y plane). The system could be considered to be an infinite thin plate (typically $t_s / \sum t_{c,kj} > 100$). In such case, its bending results in an equal biaxial in-plane stress, i.e. $\sigma_x = \sigma_y$. Moreover, all materials are considered to be isotropic.

3.2. Model definition

The multilayer coating is deposited by chemical vapor deposition technique on a metallic substrate. During its normal use in solar receivers, the coating/substrate system is subjected to thermal cycling under air between room

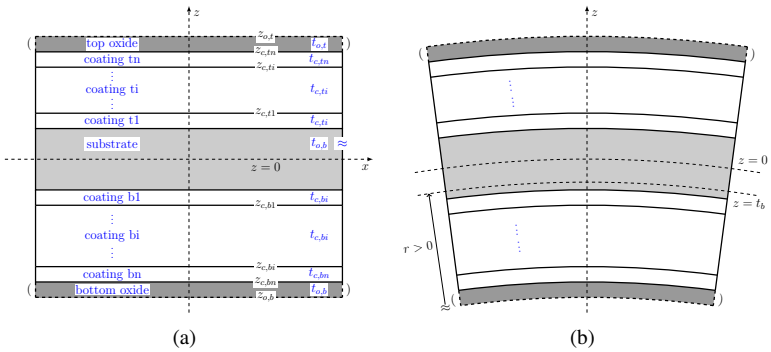

Figure 1: Schematic representation of the multilayer coating system: (a) a typical stress-free multilayer coating system; and (b) bending of the system induced by asymmetric stresses, leading to a convex curvature.

temperature and a high temperature plateau followed by an holding time at this temperature during several hours (duration of sun exposure). Under such conditions, stresses will be developed in the system. Four contributions are modeled in the present work : residual stress induced by the coating deposition (CVD), thermal gradient in the multilayer coating system during its use in solar receivers, creep deformation and high temperature oxidation. Each of these contributions are detailed below.

3.2.1. Residual stress induced by CVD

Prior to the CVD deposition of the AlN coating, we assume an initial stress-free state for the substrate at the deposition temperature and a uniform temperature field within the system during deposition. Polycrystalline films usually grow through the nucleation of discrete crystal clusters or islands on the substrate surface. Successive stages including the growth of islands, impingement of islands and their coalescence take place to form a continuous surface, and thus grain boundaries. The film thickness just after islands coalescence is usually of the order of 30 nm or less [12]. Subsequently, the film evolves by grain coarsening and grain growth, which leads to further thickening [13]. The evolution of growth stresses through these complex stages is not yet fully understood. However, for a given process, the growth stresses are usually reproducible and the final values remain constant at ambient temperature for a long time [14]. Therefore, it is assumed that the value of growth stress is constant for each coating (or film), and uniform throughout the thickness of the corresponding layer.

In the present study, we suppose an elastic relationship between the growth stress and strain, as:

$$\sigma_{c,g,i} = -\frac{E_{c,i}}{1-\nu_{c,i}} \cdot \epsilon_{c,g,i} \tag{3}$$

where $E_{c,i}$ and $\nu_{c,i}$ are the Young's modulus and Poisson's ratio of coating i respectively. $\sigma_{c,g,i}$ is the final growth stress for coating i, $\epsilon_{c,g,i}$ is the corresponding strain. The opposite sign between stress and strain is due to the substrate constraint. For the following analysis, σ >0 denotes tensile stress while σ <0 denotes compressive stress.

Stresses arising from changes in physical environment also contribute to residual stress distribution within the system. Different from the growth stresses, such externally induced stresses are commonly referred to as extrinsic stresses. Generally, only the thermal stress is taken into account. The thermal stress is a consequence of thermal strain mismatches due to different thermal expansion coefficients of layers and the temperature fluctuation from the deposition temperature (T_{growth}) to ambient temperature (T_{final}). For each layer, i, the thermal strain, $\epsilon_{th,i}$, is written as:

$$\epsilon_{th,i} = \int_{T_{growth}}^{T_{final}} \alpha_i(T)dT \tag{4}$$

where α is the temperature dependent thermal expansion coefficient, T_{growth} and T_{final} denote the deposition and final temperature (generally equal to ambient temperature) of CVD growth respectively.

Based on classical beam theory, Hsueh [15] assumed that the total strain of the system could be decomposed into a uniform strain to maintain displacement compatibility and a bending moment induced by asymmetric stresses. The total strain is thus described as:

$$\epsilon = c + \frac{z - t_B}{r} \tag{5}$$

where c is the uniform strain, z=t_B the position of the bending axis and r the radius of curvature. In Hsueh's definition [15], r is positive when the curvature of system (1/r) is convex, and vice versa (1(b)). The same formalism is used here. The biaxial residual stresses in each coating (or film) and in the substrate are expressed as:

$$\sigma_{c,i} = \frac{E_{c,i}}{1 - \nu_{c,i}}(c + \frac{z - t_B}{r} - \epsilon_{c,g,i} - \epsilon_{c,th,i}) \tag{6a}$$

$$\sigma_s = \frac{E_s}{1 - \nu_s}(c + \frac{z - t_B}{r} - \epsilon_{s,th}) \tag{6b}$$

where E is the Young's modulus, and ν the Poisson's ratio of materials. The stress distribution within the system is depending on the three unknown parameters c, t_b, and r, which can be determined upon three boundary conditions [15]. The details are given below.

3.2.2. Thermal gradient in the multilayer

The previous section describes the stress inherent to the deposition of the coatings by CVD. In the following, we consider stress arising from the use of the system (CVD grown layers and substrate) under solar radiation. Here, we consider a general case in which the multilayer coating system is subjected to an imposed heat flux, q, at the top surface only . The top and bottom surfaces of the system are rapidly heated up to different temperatures T_t and T_b respectively. To simplify the problem, we assume that (1) the heat transfer within the system during the thermal cycling is only steady-state conduction; (2) no interface, convection and thermal radiation resistance exist; (3) the heat flux is maintained constant during the thermal cycle; and (4) the temperature of heat transfer fluid is the same as the temperature at the bottom surface (i.e., T_{HTF}=T_b).

According to the Fourier's law, for the multilayer coating system illustrated in 1, the relationship between the heat flux q and the surface temperatures can be expressed as:

$$\begin{gathered} q = -\frac{T_t(t) - T_b(t)}{R_{total}(t)} \\ R_{total}(t) = \frac{t_s(t)}{\lambda_s} + \frac{t_{o,t}(t)}{\lambda_{o,t}} + \frac{t_{o,b}(t)}{\lambda_{o,b}} + \sum_{i=1}^{n} \frac{t_{c,ti}(t)}{\lambda_{c,ti}} + \sum_{i=1}^{m} \frac{t_{c,bi}(t)}{\lambda_{c,bi}} \end{gathered} \tag{7}$$

where T_t(t) and T_b(t) are time-dependent temperatures at the top and bottom surfaces respectively. R_{total} is the total thermal resistance of the system and λ the thermal conductivity. It is assumed that thermal conductivities are constant during thermal cycling. Then, we can derive the temperature at the position z for a given time t:

$$T(z,t) = \begin{cases} T_b(t) + q\frac{z_{o,b}(t) - z}{\lambda_{o,b}} & z_{o,b}(t) < z \leq z_{c,bm}(t) \\ T_b(t) + q(\frac{-\frac{t_s(t)}{2} - z_{c,bi}(t) - z}{\lambda_{c,bi}} - \sum_{j=i+1}^{m} \frac{t_{c,bj}(t)}{\lambda_{c,bj}} - \frac{t_{o,b}(t)}{\lambda_{o,b}}) & z_{c,bi}(t) < z \leq z_{c,b(i-1)}(t) \\ T_b(t) + q(\frac{-\frac{t_s(t)}{2} - z}{\lambda_s} - \sum_{i=1}^{m} \frac{t_{c,bi}(t)}{\lambda_{c,bi}} - \frac{t_{o,b}(t)}{\lambda_{o,b}}) & \frac{-t_s(t)}{2} < z \leq \frac{t_s(t)}{2} \\ T_b(t) + q(\frac{\frac{t_s(t)}{2} + z_{c,t(i-1)}(t) - z}{\lambda_{c,ti}} - \frac{t_s(t)}{\lambda_s} - \sum_{i=1}^{m} \frac{t_{c,bi}(t)}{\lambda_{c,bi}} - \frac{t_{o,b}(t)}{\lambda_{o,b}}) & z_{c,t(i-1)}(t) < z \leq z_{c,ti}(t) \\ T_b(t) + q(\frac{z_{o,t}(t) - z}{\lambda_{o,t}} - R_{total}(t) + \frac{t_{o,t}(t)}{\lambda_{o,t}}) & z_{c,tn}(t) < z \leq z_{o,t}(t) \end{cases} \tag{8}$$

As it is described after, the thickness of the system will vary during the thermal cycling due to the oxidation of coatings at high temperature. Therefore, the temperature field, T(z,t) is redistributed at each time step.

3.2.3. Creep deformation

In the present study, to simplify the model, the secondary creep stage is assumed during thermal cycling since a large fraction of the creep life is within this stage [16]. Based on Norton's power law [17], a largely phenomenological, macroscopic relationship between steady-state creep rate, $\dot{\epsilon}_{cr}$, and corresponding stress, σ_{cr}, is expressed as follows:

$$\dot{\epsilon}_{cr} = sign(\sigma_{cr}) \cdot A \cdot exp(-\frac{Q_{cr}}{kT}) \cdot \sigma_{cr}^{n} \tag{9}$$

where A is the creep prefactor, k is the Boltzmann's constant, Q_{cr} is the activation energy for creep, and n is the creep exponent. Q_{cr} is often found to be the activation energy of lattice self-diffusion [16]. The sign function $sign(\sigma_{cr})$ is defined as $\sigma_{cr}/|\sigma_{cr}|$.

We assumed that heating and cooling periods are relatively short compared to the holding period, i.e., 10 h of holding time and less than 1 min of heating and cooling. Therefore, creep behavior is neglected during the heating and cooling periods, and the creep strains accumulate only during the high temperature plateau. Moreover, creep is considered in all the elements of the structure: the coatings, growing oxide scales and substrate. The instantaneous creep strain at z coordinate, $\epsilon_{cr}(z,t)$, is written as:

$$\epsilon_{cr}(z, t + dt) = \epsilon_{cr}(z, t) + \dot{\epsilon}_{cr}(z, t) \cdot dt \tag{10}$$

Here also, the creep strain is recalculated for each time step due to the evolution of the system structure and the stress field during thermal cycling.

3.2.4. High temperature oxidation

During the high temperature exposure under air, oxidation takes place. Oxide scales are formed at the outer surfaces of the system. The growth of scales is accompanied by the generation of a large residual stress due to the intrinsic oxide growth strain in the lateral direction, resulting in the redistribution of the stress field in the system. Based on our previous study, we assume a linear oxidation behavior for AlN [8]

When the oxidation is controlled by a surface reaction, the oxide scale grows linearly. We assumed that in this analysis the lateral growth strain in the oxide, $\epsilon_{o,l}$, is constant when oxidation follows linear kinetics, with a value of $\epsilon_{o,l}$=0.001 deduced from our experiments. Furthermore, when the oxide scale grows, the coating thickness decreases. Assuming an isotropic behavior for both coating and substrate, the decreasing thickness of the oxidized coating can be expressed as:

$$-dt_{coating} = (\frac{\Omega_{coating}}{\Omega_{oxide}})^{\frac{1}{3}} \cdot dt_{oxide} \tag{11}$$

where $\Omega_{coating}$ and Ω_{oxide} are the volume of coating and oxide per metal ion respectively.

3.2.5. Summary of assumptions

The aforementioned assumptions are:

- Initial stress-free state for substrate at deposition temperature, and a uniform temperature field in the coatings/substrate system during deposition;
- Temperature field in the system is assumed to be uniform at ambient temperature;
- Steady-state thermal conduction within the system when it is subjected to thermal loading;
- Secondary creep and oxidation take place only at high temperature, and are neglected during the heating and cooling periods;
- Creep strain accumulates following Norton's power law;
- Constant intrinsic growth strain for coatings and constant thermal conductivities during thermal cycling;
- The lateral growth strain remains constant when the oxide growth is linear;
- Perfect bonding between two adjacent layers.

According to the assumptions shown above, creep strain is updated for each time step :

$$\epsilon_{cr}(z, t + \Delta t) = \epsilon_{cr}(z, t) + \dot{\epsilon}_{cr}(z, t) \cdot \Delta\tau \tag{12}$$

with

$$\Delta\tau = \begin{cases} \Delta t & \text{during the holding time at the high temperature plateau} \\ 0 & \text{during the heating and cooling process} \end{cases} \tag{13}$$

where Δt is the time increment and $\Delta\tau$ the increment of holding time. In the case of oxide growth with a parabolic law, the lateral strain, $\epsilon_{o,l}$ must also be updated for each time step (eq. 23 in Appendix A).

3.2.6. Stress evolution and simulation procedure

Following Eq. 5, the instantaneous total strain, $\epsilon(z, t)$, at the position z is expressed as:

$$\epsilon(z, t) = c(t) + \frac{z - t_B(t)}{r(t)} \tag{14}$$

where c(t), t_B(t) and r(t) are the time-dependent uniform curvature, bending axis position and radius of curvature, respectively (see Eq. 5).

Thus, the general set of equations for the calculation of biaxial stress at the position z, $\sigma(z, t)$, can be written as:

$$\begin{cases} \sigma_{o,b}(z,t) = \frac{E_{o,b}}{1-\nu_{o,b}}[\epsilon(z,t) - \epsilon_{o,th,b}(z,t) - \epsilon_{o,cr,b}(z,t) - \epsilon_{o,l,b} - \epsilon_{0,b}] & z_{o,b}(t) \leq z \leq z_{c,bm}(t) \\ \sigma_{c,bi}(z,t) = \frac{E_{c,bi}}{1-\nu_{c,bi}}[\epsilon(z,t) - \epsilon_{c,th,bi}(z,t) - \epsilon_{c,cr,bi}(z,t) - \epsilon_{c,g,bi}] & z_{c,bi}(t) \leq z \leq z_{c,b(i-1)}(t) \\ \sigma_{s}(z,t) = \frac{E_{s}}{1-\nu_{s}}[\epsilon(z,t) - \epsilon_{s,th}(z,t) - \epsilon_{s,cr}(z,t)] & \frac{-t_s(t)}{2} \leq z \leq \frac{t_s(t)}{2} \\ \sigma_{c,ti}(z,t) = \frac{E_{c,ti}}{1-\nu_{c,ti}}[\epsilon(z,t) - \epsilon_{c,th,ti}(z,t) - \epsilon_{c,cr,ti}(z,t) - \epsilon_{c,g,ti}] & z_{c,t(i-1)}(t) \leq z \leq z_{c,ti}(t) \\ \sigma_{o,t}(z,t) = \frac{E_{o,t}}{1-\nu_{o,t}}[\epsilon(z,t) - \epsilon_{o,th,t}(z,t) - \epsilon_{o,cr,t}(z,t) - \epsilon_{o,l,t} - \epsilon_{0,t}] & z_{c,tn}(t) \leq z \leq z_{o,t}(t) \end{cases} \tag{15}$$

where ϵ_{cr}, $\epsilon_{o,l}$, and ϵ_g are respectively the creep strain (eqs. (9) and (12)), the lateral growth strain and the intrinsic CVD growth strain (Eq. 3) in the coatings and the thermal strain. $\epsilon_{0,t}$ and $\epsilon_{0,b}$ represent the total strain at the top and bottom surface of system just before the formation of first layer of oxide, respectively. The instantaneous thermal strains, ϵ_{th}, are defined as the expansion due to temperature change from the temperature at which the stress-free state could be assumed to the instantaneous temperature at the position z, such as:

$$\begin{cases} \epsilon_{o,th,b}(z,t) = \int_{T_{oxide}(z)}^{T(z,t)} \alpha_{o,b}(T)dT & z_{o,b}(t) \leq z \leq z_{c,bm}(t) \\ \epsilon_{c,th,bi}(z,t) = \int_{T_{growth,bi}}^{T(z,t)} \alpha_{c,bi}(T)dT & z_{c,bi}(t) \leq z \leq z_{c,b(i-1)}(t) \\ \epsilon_{s,th}(z,t) = \int_{T_{growth,s}}^{T(z,t)} \alpha_{s}(T)dT & \frac{-t_s(t)}{2} \leq z \leq \frac{t_s(t)}{2} \\ \epsilon_{c,th,ti}(z,t) = \int_{T_{growth,ti}}^{T(z,t)} \alpha_{c,ti}(T)dT & z_{c,t(i-1)}(t) \leq z \leq z_{c,ti}(t) \\ \epsilon_{o,th,t}(z,t) = \int_{T_{oxide}(z)}^{T(z,t)} \alpha_{o,t}(T)dT & z_{c,tn}(t) \leq z \leq z_{o,t}(t) \end{cases} \tag{16}$$

T(z,t) is the instantaneous temperature at the position z (Eq. 8), T_{growth} is the CVD growth temperature and T_{oxide}(z) is the oxidation temperature (temperature of the oxidation plateau) of the oxide scale at the position z.

Three boundary conditions are used to determine the three unknown parameters c, t_b, and r :

(1) **The resultant force due to the uniform strain component is zero**, therefore:

$$\begin{aligned}
&\int_{z_{o,b}(t)}^{z_{c,bm}(t)} \frac{E_{o,b}}{1-\nu_{o,b}}[c(z,t)-\epsilon_{o,th,b}(z,t)-\epsilon_{o,cr,b}(z,t)-\epsilon_{o,l,b}(z,t)]dz \\
&+\sum_{i=1}^{m}\int_{z_{c,bi}(t)}^{z_{c,b(i-1)}(t)} \frac{E_{c,bi}}{1-\nu_{c,bi}}[c(z,t)-\epsilon_{c,th,bi}(z,t)-\epsilon_{c,cr,bi}(z,t)-\epsilon_{c,g,bi}(z,t)]dz \\
&+\int_{-\frac{t_s(t)}{2}}^{\frac{t_s(t)}{2}} \frac{E_s}{1-\nu_s}[c(z,t)-\epsilon_{s,th}(z,t)-\epsilon_{s,cr}(z,t)]dz \\
&+\sum_{i=1}^{n}\int_{z_{c,t(i-1)}(t)}^{z_{c,ti}(t)} \frac{E_{c,ti}}{1-\nu_{c,ti}}[c(z,t)-\epsilon_{c,th,ti}(z,t)-\epsilon_{c,cr,ti}(z,t)-\epsilon_{c,g,ti}(z,t)]dz \\
&+\int_{z_{c,tn}(t)}^{z_{o,t}(t)} \frac{E_{o,t}}{1-\nu_{o,t}}[c(z,t)-\epsilon_{o,th,t}(z,t)-\epsilon_{o,cr,t}(z,t)-\epsilon_{o,l,t}(z,t)]dz=0
\end{aligned} \tag{17}$$

(2) **The resultant force due to the bending component is zero**, therefore:

$$\begin{aligned}
&\int_{z_{o,b}(t)}^{z_{c,bm}(t)} \frac{E_{o,b}}{1-\nu_{o,b}}\cdot\frac{z-t_B(t)}{r(t)}dz+\sum_{i=1}^{m}\int_{z_{c,bi}(t)}^{z_{c,b(i-1)}(t)} \frac{E_{c,bi}}{1-\nu_{c,bi}}\cdot\frac{z-t_B(t)}{r(t)}dz \\
&+\int_{-\frac{t_s(t)}{2}}^{\frac{t_s(t)}{2}} \frac{E_s}{1-\nu_s}\cdot\frac{z-t_B(t)}{r(t)}dz+\sum_{i=1}^{n}\int_{z_{c,t(i-1)}(t)}^{z_{c,ti}(t)} \frac{E_{c,ti}}{1-\nu_{c,ti}}\cdot\frac{z-t_B(t)}{r(t)}dz \\
&+\int_{z_{c,tn}(t)}^{z_{o,t}(t)} \frac{E_{o,t}}{1-\nu_{o,t}}\cdot\frac{z-t_B(t)}{r(t)}dz=0
\end{aligned} \tag{18}$$

(3) **The sum of bending component with respect to the bending axis is zero**, therefore:

$$\begin{aligned}
&\int_{z_{o,b}(t)}^{z_{c,bm}(t)} \sigma_{o,b}(z,t)\cdot[z-t_B(t)]dz+\sum_{i=1}^{m}\int_{z_{c,bi}(t)}^{z_{c,b(i-1)}(t)} \sigma_{c,bi}(z,t)\cdot[z-t_B(t)]dz \\
&+\int_{-\frac{t_s(t)}{2}}^{\frac{t_s(t)}{2}} \sigma_s(z,t)\cdot[z-t_B(t)]dz+\sum_{i=1}^{n}\int_{z_{c,t(i-1)}(t)}^{z_{c,ti}(t)} \sigma_{c,ti}(z,t)\cdot[z-t_B(t)]dz \\
&+\int_{z_{c,tn}(t)}^{z_{o,t}(t)} \sigma_{o,t}(z,t)\cdot[z-t_B(t)]dz=0
\end{aligned} \tag{19}$$

Eq. 17, Eq. 18, Eq. 19 are iteratively solved with a MATLAB (MATLAB 2019a) code and the resolution of this set of equations is done by a genetic algorithm. To simplify the model, it is assumed that the increase of the oxide thickness on the high temperature plateau is small. Thus, the oxidation temperature of the top surface, $T_{t,0}$ and of the bottom surface $T_{b,0}$ are assumed to be constant on this plateau. The initial and final temperatures of each thermal cycle are defined as $T_{ambient}$=25 °C. The procedure is shown in Figure 2 and the main steps are summarized as follows:

Step 1: Initiate the multilayer coating system, $\epsilon_{cr}(z,0)=0$, and $\epsilon_{o,l}=0.001$. Impose the CVD growth strain in coating i, $\epsilon_{c,g,i}$, the deposition temperature T_{growth} and the final ambient temperature $T_{ambient}$.

Step 2: Calculate the residual stresses within the system using eqs. (4) to (6), and the three boundary conditions described in the eq. (17) to eq. (19); then, impose the heat flux q and start the thermal cycling;

Step 3: Impose a time increment Δt;

Step 4: Determine the instantaneous z coordinate, z(t), using eqs. (1), (2) and (11);

Step 5: Determine the temperature field T(z,t) within the system using Eq. 8;

Step 6: Determine the thermal strain field $\epsilon_{th}(z,t)$ using Eq. 16, update the creep strain field $\epsilon_{cr}(z,t)$;

Step 7: Solve eqs. (17) to (19) by a genetic algorithm to obtain c(t), t_b(t) and r(t);

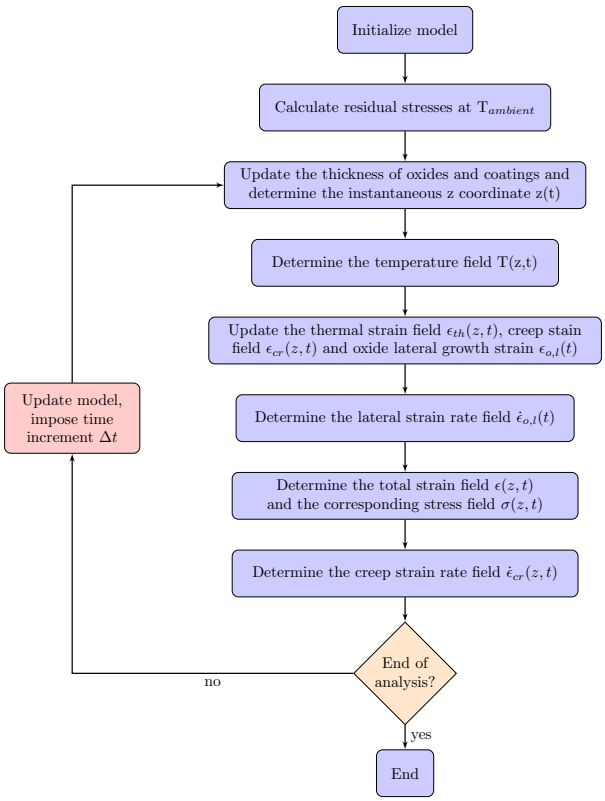

Figure 2: Flow chart of the model.

Step 8: Determine the total strain field ϵ(z,t) and the corresponding stress field σ(z,t) using eqs. (14) and (15); then update the creep strain rate field $\dot{\epsilon}_{cr}(z,t)$ for the next iteration with eq. (9);

Step 9: If it is the end of the thermal cycling, finish the analysis; otherwise, back to Step 3 for next iteration.

A comparison of results from the present analytical model and from a Finite element analysis (FEA) has been performed to verify the accuracy of the proposed analytical model. Details on the FEA model and the validation of the analytical model are given in the Supplementary Material (Figures S1-S3).

4. Results and discussion

The AlN/TZM system appears to be a potentially ideal system for solar receivers thanks to the exceptional elevated temperature strength of TZM. Also, AlN has a reasonable oxidation resistance [8] and has a thermal expansion coefficient close to the one of TZM. Therefore, such multilayer system is used for the following discussion, Figure 3(a). The 1-mm-thick TZM substrate is covered on all faces with a 60-µm-thick polycristalline AlN coating. Materials parameters are given Table 1. The residual stress at room temperature induced by CVD deposition has been estimated to 1290 MPa ($\epsilon_{c,g}$=-0.003) according to the $\sin^2\psi$ method. A discussion on the residual stress in AlN coatings and its effect on global stress evolution during thermal cycling is given in the Supplementary Material (Figure S6). The simulation is performed for ten cycles, one cycle corresponds to ten hours.

4.1. Effect of oxidation

The heat transfer fluid and the heat flux are respectively set to 1000°C and 10 MW·m^{-2}. Such boundary conditions leads to a temperature difference of 137°C between the the top and bottom surface of the system. When the oxide scale growth is taken into account, the geometry of the system will evolve with time due to consumption of the AlN layer and the growth of the corresponding alumina. The thickness of the oxide scales and coatings versus time are

Table 1
Material properties of TZM, AlN and Al_2O_3 used in the complete model.

Properties	TZM	AlN	Al_2O_3	Reference
Young's modulus E (GPa)	320	340	379	[6]
Poisson's ratio ν	0.3	0.21	0.25	[6]
Thermal conductivity λ ($W{\cdot}m^{-1}{\cdot}K^{-1}$)	103.5	30	10	[18, 19]
Thermal expansion coefficient α ($10^{-6}{\cdot}{}^{\circ}C^{-1}$)	fifth-order fitting: $\alpha = \sum_{i=0}^{5} B_i T^i$			[20]
B_0 ($10^{-6}{\cdot}{}^{\circ}C^{-1}$)	5.171	2.474	5.077	
B_1 ($10^{-6}{\cdot}{}^{\circ}C^{-2}$)	-5.918×10^{-3}	1.117×10^{-2}	1.432×10^{-2}	
B_2 ($10^{-6}{\cdot}{}^{\circ}C^{-3}$)	3.522×10^{-5}	-1.328×10^{-5}	-2.305×10^{-5}	
B_3 ($10^{-6}{\cdot}{}^{\circ}C^{-4}$)	-5.012×10^{-8}	8.680×10^{-9}	2.064×10^{-8}	
B_4 ($10^{-6}{\cdot}{}^{\circ}C^{-5}$)	3.164×10^{-11}	-2.950×10^{-12}	-8.839×10^{-12}	
B_5 ($10^{-6}{\cdot}{}^{\circ}C^{-6}$)	-7.078×10^{-15}	4.057×10^{-16}	1.425×10^{-15}	
Creep exponent n	3.03	1	1.65	[21]
Creep prefactor A ($MPa^{-n}{\cdot}s^{-1}$)	1.796×10^{3}	2.928×10^{10}	6.472×10^{6}	[21]
Creep activation energy Q_{cr} ($kJ{\cdot}mol^{-1}$)	481	586	460	[21]
Oxidation kinetics	/	linear	$\epsilon_{o,l}$=0.001	Experiment
Oxidation pre-exponential factor k_0 ($mg{\cdot}cm^{-2}{\cdot}h^{-1}$)	/	35.92	/	Experiment
Oxidation activation energy E_a($J{\cdot}mol^{-1}$)	/	9.732×10^{4}	/	Experiment
Volume per Al ion Ω (m^3)	/	2.091×10^{-29}	2.132×10^{-29}	[22]

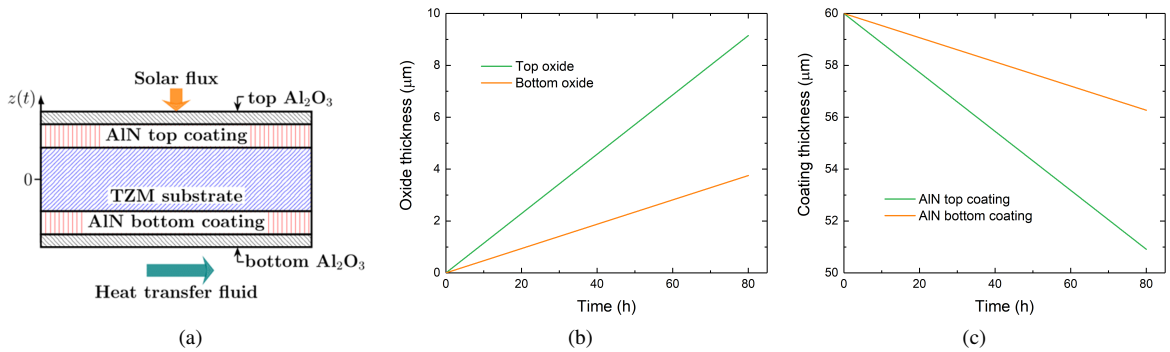

Figure 3: (a) Schematic representation of the AlN/TZM system during operation and thickness evolution of the (b) oxide scales and (c) AlN coatings on the front-side and backside of system.

presented in Figure 3. Due to the temperature difference established in the system, the oxide growth rate at the top surface of the system is 2.5 times higher than that at the bottom surface.The thickness exchange factor (from AlN to Al_2O_3, eq. (11)) is around 1.01. Therefore, the increase of the total thickness of the system due to oxide scale growth is not significant. However, the transformation from thermal conductive AlN to less thermal conductive Al_2O_3 leads to a redistribution of the temperature field and related thermal strain field during thermal cycling. As illustrated in Figure 4, the temperature in both coatings and substrate increases with the time. Due to the growth of oxide scale, the temperature at the top surface of the system is 12 °C higher after 10 thermal cycles. Although it might not be significant for short high oxidation exposure, it could become relevant for longer time since the creep strain will be redistributed due to this temperature evolution according to the Norton's creep power law (Eq. 9).

Figure 5 presents the time evolution of bending curvature with non-growing and growing oxide scale during ten cycles. Within one cycle (i.e. label 1 to 3), the system goes from a non curved state at room temperature to a concave shape during heating up to the high temperature plateau and return back to a a slightly convex shape during cooling. Indeed, the large temperature change leads to a significant enhancement of thermal strain mismatches between the AlN coatings and the substrate. To compensate such mismatches, the bending strain is strongly reduced to maintain the

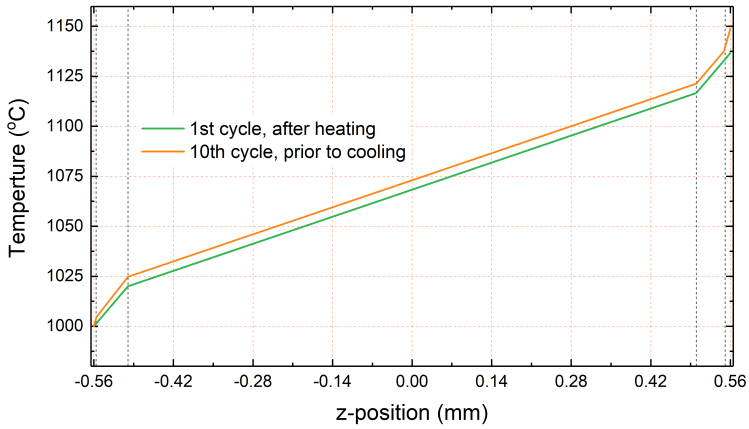

Figure 4: Temperature redistribution due to the oxidation of AlN coatings.

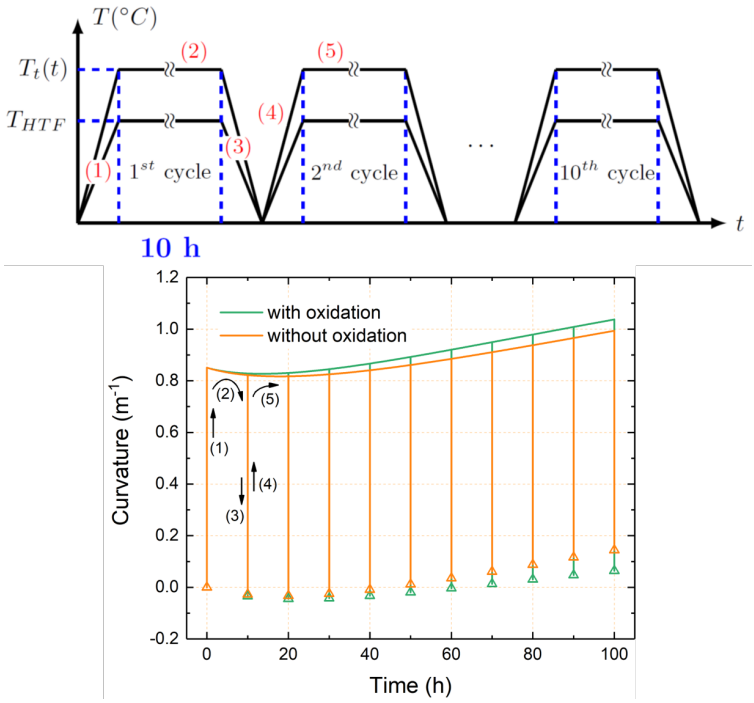

Figure 5: Evolution of the curvature of the system with and without oxidation. Triangles represent the value at ambient temperature

system equilibrium. Additionally, the curvatures at the high temperature plateau decrease with exposure time at the beginning of thermal cycling, followed by an increase of the curvature. The oxidation of AlN has almost no influence on the curvature.

In order to understand such behaviour, the evolution of stresses and creep strains in the growing oxide scale, AlN coatings and substrate is investigated, as plotted in Figure 6. Figure 6(a) represents the spatial evolution of stress on the high temperature plateau during the thermal cycling. Globally, the stresses in both AlN coatings and substrate are almost unaffected by the presence of growing oxide scales (see Figure S4 in the Supplementary Material). Top and bottom AlN coatings are in tension during the thermal cycling with a value around 1000 MPa during the first cycle. The substrate is under compression with a value around -120 MPa. During thermal cycling, the top AlN coating undergoes creep relaxation and the stress decreases to 550 MPa after 10 cycles, while the stress in the bottom AlN

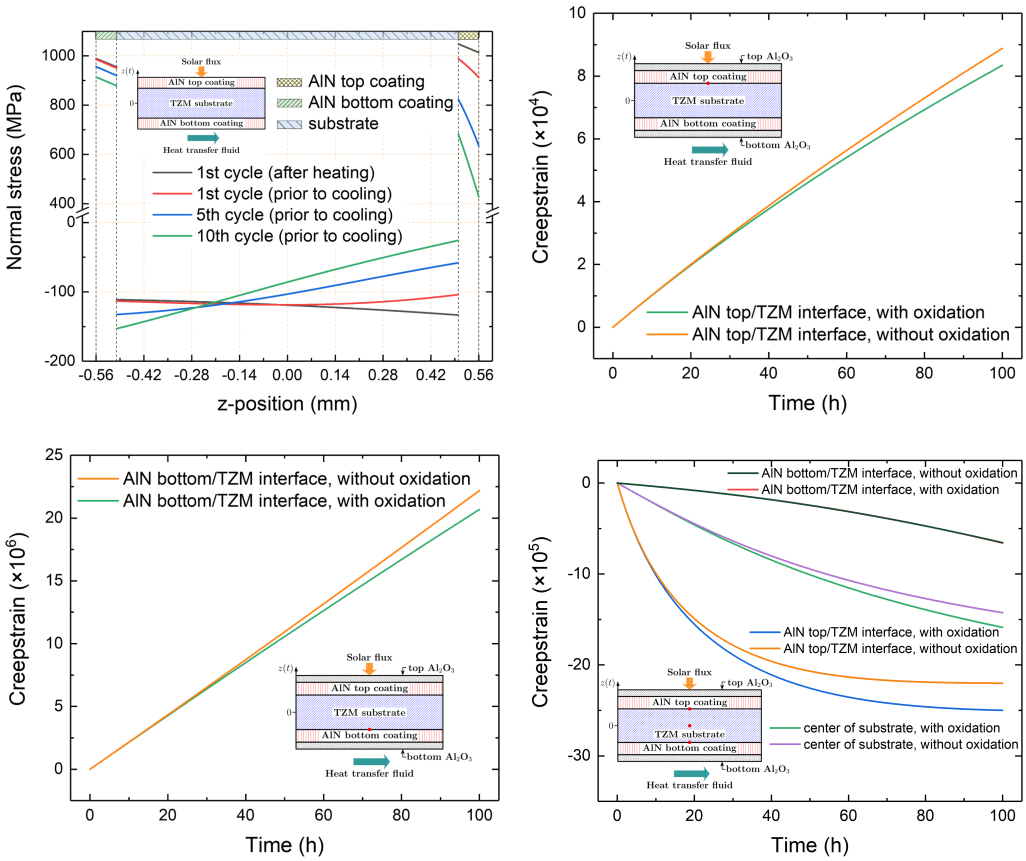

Figure 6: (a) Normal stress distribution in the system during thermal cycling. Effect of oxidation on the creep strain on the high temperature plateau in (b) top AlN coating, (c) bottom AlN coating and (d) the substrate.

coating decreases only to 900 MPa. As the creep deformation rate is a function of material temperature (Eq. 9), and the bottom AlN coating is cooler than the top AlN coating, the development and accumulation of creep strain in the top AlN coating is more significant. Stress in the top coating is therefore rapidly relaxed. This is further illustrated with Figure 6(c) and Figure 6(b) where the creep strain is plotted versus time. The creep strain in the top AlN coating is two order of magnitude higher than in the bottom coating. In the thick substrate, fast stress relaxation and creep saturation takes place at the AlN top coating/substrate interface (z=0.5 mm), while stress accumulation and acceleration of creep strain is observed at the AlN bottom coating/substrate interface (z=-0.5 mm, Figure 6(d)). The stress relaxation at the AlN top coating/substrate interface reduces the corresponding creep strain rate, which in turn, decelerates the following stress relaxation. Such a negative feedback leads to a saturation of creep strain. On the contrary, compressive stress at the AlN bottom coating/substrate interface slightly increases during the first thermal cycle. This stress accumulation results in an increase of creep strain rate. As time extends, the generation of irreversible creep strain accelerates, resulting in an increase of stress. Therefore, the slope of stress distribution is reversed from negative to positive due to such asymmetric evolution on both surfaces of the substrate (Figure 6(a)) during the first cycle and the stress gradient in the system is further strengthened with the number of cycle. This enhancement of the system asymmetry explain the increase in curvature as observed in Figure 5. Finally, the different oxide growth rate at the top and bottom AlN coatings reinforce the system asymmetry which give a slightly higher curvature value.

4.2. Effect of heat flux on the front side

The heat flux q is varied from 0.5 to 10 MW·m^{-2} to illustrate the effect of temperature gradients on the stress evolution. The q=0.5, 1 and 10 MW·m^{-2} are adopted to represent the low, medium (realistic) and extremely high thermal load during thermal cycling. The temperature of the heat transfer fluid is 1000°C and the oxide growth scale

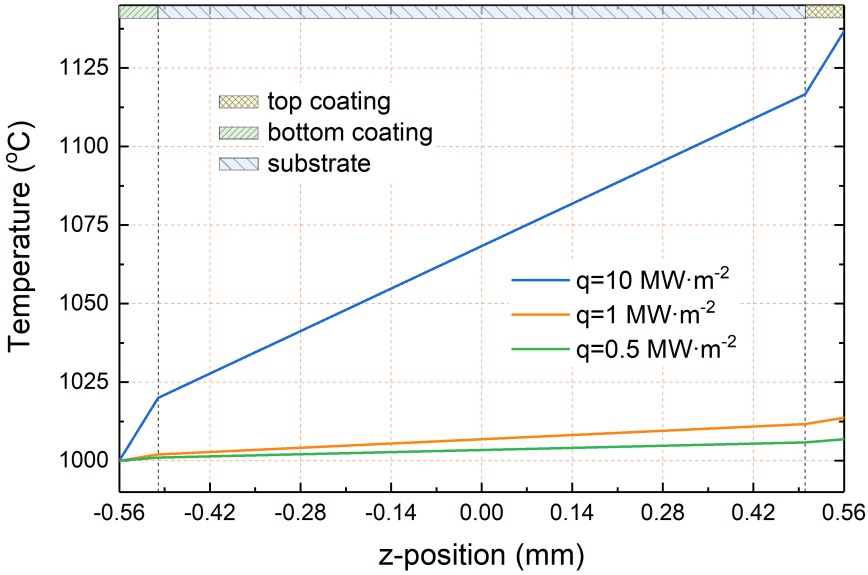

Figure 7: Temperature distribution along the z direction when the system is subjected to different solar heat fluxes.

is considered.

As shown in Figure 7, the initial temperature difference (just after heating in the first cycle) in the system is 137, 14 and 7 °C for a heat flux of 10, 1 and 0.5 MW·m^{-2} respectively. For 10 MW·m^{-2}, the large temperature difference within the system gives rise to the asymmetrical evolution of stress and creep strain as discussed previously. By contrast, the overall temperature difference can be neglected (less than 15 °C after 10 thermal cycles) when the imposed heat flux is low ($\leqslant$1 MW·m^{-2}). The corresponding difference of creep strain rate is also reduced in each individual layer, and the stress evolution on both side of the system can be consider symmetric. As a result, the curvature remains nearly constant with a low value (below 0.1 m^{-1}), as illustrated in Figure 8(a).

For all cases, large compressive stresses are developed in the oxide scale just after heating in the first cycle, around -515 MPa (Figure 8(b)). As time increases, creep strains develop in the top (z>0) and bottom (z<0) oxides and leads to a stress relaxation in both oxide scales. As a result, the stress on the high temperature plateau reach almost zero after 10 cycles. However, the stress is tensile (> 600 MPa) at ambient temperature due to the higher thermal expansion coefficient of Al_2O_3. Such large stresses may induce cracks, interfacial delamination and/or spallation of oxides. This phenomenon suggests that the design of a multilayer system should account for stresses at both high temperature and ambient temperature as the opposite sign of stress can affect the system durability in different ways [7].

In the AlN top coating, stresses evolve nearly elastically (up to 930 MPa on the high temperature plateau) with a low heat flux ($\leqslant$1 MW·m^{-2}). When the imposed heat flux is higher, the higher temperature in the top coating gives rise to higher creep strain and a more significant stress relaxation (Figure 8(c)). Same trends have been observed for stress at the center of substrate (Figure 8(d)). Moreover, for heat fluxes of 1 and 0.5 MW·m^{-2}, the stress gradient within the thick substrate is negligible, while a high heat flux of 10 MW·m^{-2} generate a complex evolution of stress field in the substrate as discussed in the previous section.

4.3. Effect of heat transfer fluid temperature

The heat flux is considered to be constant with a value of 1 MW·m^{-2} in the following analysis. Three different heat transfer fluid temperatures, 900, 1000 and 1100 °C, are selected in the current analysis to illustrate the influence of the targeted heat transfer fluid temperature (T_{HTF}). The temperature difference within the system is less than 15°C for these three cases. The corresponding temperatures at the top and bottom surfaces are given Table 2.

Figure 9(b) summarizes the evolution of curvature and stress at the three representative positions as a function of the heat transfer fluid temperature. The curvature is strongly affected by the heat transfer fluid temperature. For T_{HTF} of 900°C and 1000°C, the curvature remains nearly constant with a low value (below 0.08 m^{-1}.) while the curvature decreases and subsequently raises for T_{HTF} of 1100 °C. Indeed, while increasing T_{HTF}, despite the insignificant

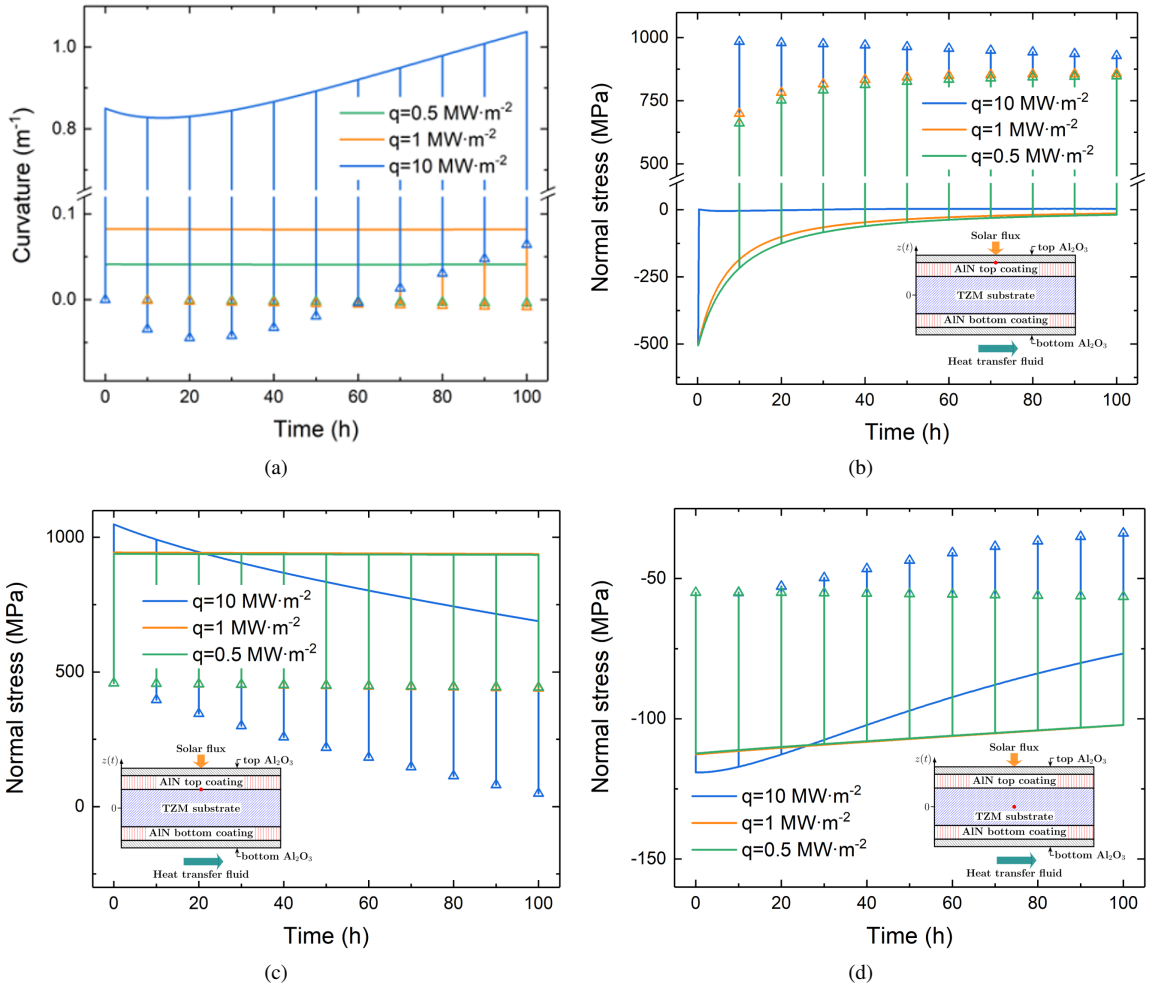

Figure 8: Effect of heat fluxes on (a) evolution of the curvature, and stress evolution at (b) oxide/AlN top coating interface (on oxide side), (c) AlN top coating/substrate interface (on coating side) and (d) the center of substrate; triangles represent the curvature and/or stresses at ambient temperature.

Table 2
Temperature at the top surface of the system and the thickness of the top and bottom oxide scales after 10 thermal cycles.

T_b (°C)	T_t (°C)	Thickness (μm)	
		Top oxide	Bottom oxide
900	914	2.4	2.1
1000	1014	5.2	4.7
1000	1115	10.0	9.2

temperature difference, the reduce of stress gradient in the thick substrate is accelerated due to the larger creep strain (higher temperature). Stresses are rapidly redistributed, leading to the sign change of the stress distribution slope. Stress gradient is subsequently enhanced as discussed previously. As a result, the curvature increases.

Figures 9(b)-9(d) show the stress evolution at the three representative positions. As expected, the high T_{HTF} leads to the fast stress relaxations in each individual layer because of temperature dependence of creep strain rate. These findings are consistent with the discussions given before. For T_{HTF} of 1000 °C, it is interesting to note that stress in the oxide scale relaxes while the evolution of that in both AlN top coating and substrate remains nearly elastic. This

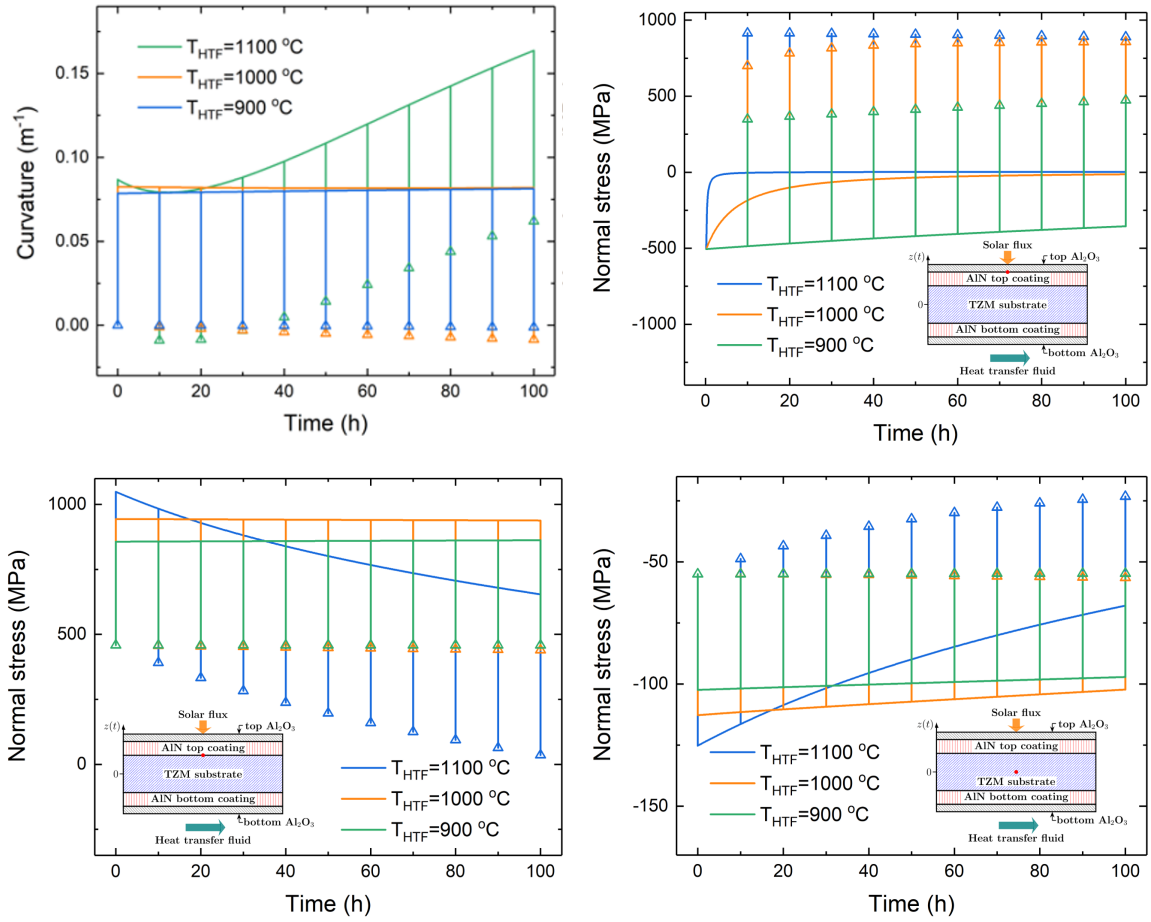

Figure 9: Effect of temperature at the bottom surface on (a) evolution of the curvature of the system, and stress evolution at (b) oxide/AlN top coating interface (on oxide side), (c) AlN top coating/substrate interface (on coating side) and (d) the center of substrate; triangles represent the curvature and/or stresses at ambient temperature.

can be explained by the better creep resistance of AlN and TZM. Nevertheless, the faster relaxation of stress, however, results in larger tensile stress at ambient temperature in oxide scale (260 MPa and 950 MPa respectively for 900°C and 1000°C).

In spite of small thermal mismatches between AlN, TZM and Al_2O_3, cooling at the end of each thermal cycle gives rise to a reversal of stress in oxide from compressive to tensile.

4.4. Assessment of creep properties

We have investigated various factors in the previous sections to study how the daily operation in solar receivers alter the stress evolution within a multilayer coating system. The above discussions show that the use of a refractory-based alloy as substrate can induce huge tensile stress in the oxide scales during the cooling stage. This is due to its lower thermal expansion coefficient than that of Al_2O_3. In this section, we consider the relatively slow-creeping FeCrAl alloy, APMT, as the substrate. As it has a larger thermal expansion coefficient, compressive stress are introduced in the oxide scales during the cooling stage.

We also compared the experimental measurements and stress predicted by the proposed analytical model. The thermomechanical properties of APMT are summarized in Table 3. Due to the lack of creep properties for APMT, we herein use the creep parameters of another ODS FeCrAl alloy (MA956) for the calculations [6].

Figure 10 depicts the evolution of stresses at ambient temperature in the top oxide and AlN top coating by experimental measurements (blue points and curves) and model calculations (orange and green curves). The orange

Table 3
Material properties of APMT used in the model.

Properties	Values	Reference
Young's modulus (GPa)	220	[23]
Poisson's ratio	0.3	[23]
Thermal conductivity ($W \cdot m^{-1} \cdot K^{-1}$)	27	[23]
Thermal expansion coefficient (K^{-1})	fifth-order fitting	[23, 24]
B_0	10.768 K^{-1}	
B_1	4.059×10^{-3} K^{-2}	
B_2	-5.860×10^{-8} K^{-3}	
B_3	-6.174×10^{-9} K^{-4}	
B_4	1.065×10^{-11} K^{-5}	
B_5	4.569×10^{-15} K^{-6}	
Creep exponent n	4.98	[25]
Creep prefactor A ($MPa^{-n} \cdot s^{-1}$)	78.978	[25]
Creep activation energy ($J \cdot mol^{-1}$)	4.530×10^5	[25]
Oxidation kinetics	parabolic	[6]
Oxidation constant k_p ($m^2 \cdot s^{-1}$)	2.366×10^{-17}	[6]
lateral growth strain rate constant	4.250×10^4	[6]

curves represent the calculation using creep properties of AlN listed in Table 1, while the green curve represents the calculations assuming a fast-creeping AlN (A_c=2.928×10^{13} $MPa^{-n} \cdot s^{-1}$). For the oxide scale, results obtained by the current model are in good agreement with experimental data with a shift of around -0.5 GPa. The stress decreases gradually with the increase of oxidation time. On the contrary, the slow-creeping AlN leads to a gradual decrease of stress (orange curve in Figure 10(b)), which is in contradiction with experimental measurements. However, when AlN creeps faster (green points and curve), the feature of stress evolution is similar to that of experimental results, but there still exists an offset of around 0.5 GPa. This indicates that the creep parameters used in the model is not sufficiently accurate. In reality, AlN creeps faster. It is also suggested that the creep properties of AlN are related to its grain size [26]. This is one of the key points to be addressed in a future study.

Moreover, it should be pointed out here that, unlike the previous analysis using TZM as the substrate, large compressive stresses are introduced into the oxide scales and AlN coatings during the cooling stage because the thermal expansion coefficient of APMT is much larger. The steady stress evolution in the oxide scale and the coating ($\geq$10 h) indicate that stresses at high temperature are fully relaxed and tend to be stable. Therefore, the stresses at ambient temperature is solely determined by the thermal mismatches within the system. The offset between experimental results and model calculations, however, is mainly due to the use of inaccurate thermal expansion coefficients.

5. Conclusion

With the analytical model developed in this study, we have investigated the durability of the multilayer system for its use in solar receivers. In operation, multiple high temperature phenomena like oxidation and creep relaxation occur. The numerical tool developed in this work can help to understand the complex interplay of these phenomena in all the materials involved.

Our observations suggest that variations of curvature are not only determined by the temperature difference (related to the imposed heat flux), but the temperature in the material (which determines the creep strain and oxidation rate) as well. In general, employment of a low to medium heat flux and/or a low to medium heat transfer fluid temperature helps in maintaining the curvature in an acceptable interval (< 0.1 m-1) in the duration investigated (100 h) and therefore increasing the durability of the multilayer system. Additionally, the thermal mismatches between the oxide, coating, and substrate should be reduced as much as possible. The choice of material having smaller thermal expansion (than the oxide) as the substrate will lead to a tensile residual stress in the oxide at ambient temperature, which is considered to cause cracking and spallation of the oxide scale.

Finally, with the possibility to optimize the multilayer design (materials, architecture) in order to minimize the stress evolution, the present comprehensive model can contribute to improve the durability and performance of the

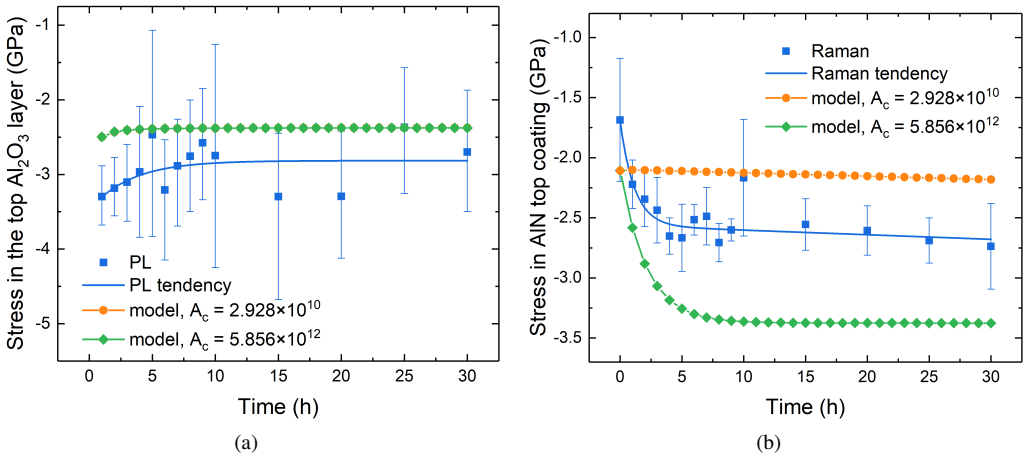

(a) (b)

Figure 10: Measured (blue points and curves) and calculated (orange and green curves) stresses at ambient temperature in (a) the top oxide and (b) AlN top coating; the residual stresses in top oxide and AlN top coating are measured by photoluminescence and Raman spectroscopy respectively (section 3.6.4).

future CSP plants.

Acknowledgements

The authors want to thank Region Auvergne-Rhône-Alpes and the Agence Nationale de la Recherche (National Agency for Research) of the French State under awards number 16005623 01-ARC4-Energies and ANR-16-CE08-0019 2MAC-CSP respectively for supporting the development of this study.

6. References

A. Case of oxide growth with a parabolic law

In the case of diffusion-controlled oxidation, the oxide growth follows a parabolic law such as:

$$t_o = k_p \cdot t^{\frac{1}{2}} \tag{20}$$

where k_p is the kinetic constant, and t is the oxidation time. t_o is defined in the previous sections as the oxide scale thickness.

During isothermal oxidation, the oxide scale freely grows in the lateral direction as well as thickening if the adjacent layer does not impose any constraint. Since the oxide is not free to expand laterally, the oxide scale is constrained and in-plane stresses are induced [27]. The lateral growth strain corresponds to the expansion of the oxide scale in the lateral direction under hypothetical stress-free conditions. In the case of diffusion controlled oxidation of metals, Rhines and Wolf [28] pointed out that the counter-current diffusion of cations and anions leads to the formation of new oxide along grain boundaries lying perpendicular to the interface. This results in the generation of lateral strain. The addition of very thin extra scale can generate large stresses [28]. If the oxide is formed at the oxide/alloy interface (location B) or outer-surface (location C), no lateral strain will be created. Based on the work of Rhines and Wolf [28], Clarke [29] developed a model using edge dislocation climb process to model the lateral growth strain. The model predicts the linear relationship between lateral strain rate, $\dot{\epsilon}_{o,l}$, and oxide thickening rate, $\dot{t}_o$, in the absence of any stress relaxation [29]:

$$\dot{\epsilon}_{o,l} = \eta_l \cdot \dot{t}_o \tag{21}$$

where η_l is a coefficient as a function of kinetic parameters.

In the case of the oxidation of nitride ceramics, few studies have focused on the stress evolution during high temperature oxidation. Therefore, eq. 21 is extended to the oxidation of ceramic coatings in the present study. Moreover, as for creep deformation mentioned above, the oxidation is assumed to take place only during the holding period. The lateral strain is considered to be independent of the position z and uniform throughout the thickness since the thickness of the oxide scale is assumed to be very small for each time step [7]. Thus, the time-dependent lateral strain of oxide, $\epsilon_{o,l}(t)$, can be written as:

$$\epsilon_{o,l}(t + dt) = \epsilon_{o,l}(t) + \dot{\epsilon}_{o,l}(t) \cdot dt \tag{22}$$

Therefore, the lateral strain, is initially set to zero ($\epsilon_{o,l}(0) = 0$) and updated for each time step :

$$\epsilon_{o,l}(t + \Delta t) = \epsilon_{o,l}(t) + \dot{\epsilon}_{o,l}(t) \cdot \Delta\tau \tag{23}$$

Then the lateral strain rate $\dot{\epsilon}_{o,l}(t)$ field is calculated for the next iteration with eqs. (20) and (21).

A comparison of stress evolution between linear and parabolic oxide growth is given in the supplementary material (Figure S5).

References

[1] A. M. Limarga, D. S. Wilkinson, Materials Science and Engineering: A 415 (2006) 94 – 103. URL: http://www.sciencedirect.com/science/article/pii/S0921509305011883. doi:https://doi.org/10.1016/j.msea.2005.09.083.

[2] A. M. Limarga, D. S. Wilkinson, Acta Materialia 55 (2007) 189 – 201. URL: http://www.sciencedirect.com/science/article/pii/S1359645406005726. doi:https://doi.org/10.1016/j.actamat.2006.07.030.

[3] H. E. Evans, International Materials Reviews 40 (1995) 1–40. URL: https://doi.org/10.1179/imr.1995.40.1.1. doi:10.1179/imr.1995.40.1.1. arXiv:https://doi.org/10.1179/imr.1995.40.1.1.

[4] X. C. Zhang, B. S. Xu, H. D. Wang, Y. X. Wu, Journal of Applied Physics 101 (2007) 083530. URL: https://doi.org/10.1063/1.2717551. doi:10.1063/1.2717551. arXiv:https://doi.org/10.1063/1.2717551.

[5] Q.-Q. Chen, F.-Z. Xuan, S.-T. Tu, Journal of Applied Physics 106 (2009) 033512. URL: https://doi.org/10.1063/1.3191684. doi:10.1063/1.3191684. arXiv:https://doi.org/10.1063/1.3191684.

[6] X. Dong, X. Feng, K.-C. Hwang, Journal of Applied Physics 112 (2012) 023502. URL: https://doi.org/10.1063/1.4736934. doi:10.1063/1.4736934. arXiv:https://doi.org/10.1063/1.4736934.

[7] B. Li, X. Fan, K. Zhou, T. Wang, International Journal of Mechanical Sciences 135 (2018) 31 – 42. URL: http://www.sciencedirect.com/science/article/pii/S0020740317318222. doi:https://doi.org/10.1016/j.ijmecsci.2017.11.010.

[8] D. Chen, J. Colas, F. Mercier, R. Boichot, L. Charpentier, C. Escape, M. Balat-Pichelin, M. Pons, Surface and Coatings Technology 377 (2019) 124872. URL: http://www.sciencedirect.com/science/article/pii/S0257897219308369. doi:https://doi.org/10.1016/j.surfcoat.2019.07.083.

[9] S. Yang, R. Miyagawa, H. Miyake, K. Hiramatsu, H. Harima, Applied Physics Express 4 (2011) 031001. URL: https://doi.org/10.1143%2Fapex.4.031001. doi:10.1143/apex.4.031001.

[10] E. Shillington, D. Clarke, Acta Materialia 47 (1999) 1297 – 1305.

[11] R. J. Christensen, D. M. Lipkin, D. R. Clarke, K. Murphy, Applied Physics Letters 69 (1996) 3754 – 3756. URL: https://doi.org/10.1063/1.117182. doi:10.1063/1.117182. arXiv:https://doi.org/10.1063/1.117182.

[12] R. Boichot, D. Chen, F. Mercier, F. Baillet, G. Giusti, T. Coughlan, M. Chubarov, M. Pons, Coatings 7 (2017). URL: https://www.mdpi.com/2079-6412/7/9/136. doi:10.3390/coatings7090136.

[13] C. V. Thompson, Annual Review of Materials Science 30 (2000) 159 – 190. URL: https://doi.org/10.1146/annurev.matsci.30.1.159. doi:10.1146/annurev.matsci.30.1.159. arXiv:https://doi.org/10.1146/annurev.matsci.30.1.159.

[14] L. B. Freund, S. Suresh, Thin Film Materials: Stress, Defect Formation and Surface Evolution, Cambridge University Press, 2004. doi:10.1017/CBO9780511754715.

[15] C. Hsueh, Thin Solid Films 418 (2002) 182 – 188. URL: http://www.sciencedirect.com/science/article/pii/S0040609002006995. doi:https://doi.org/10.1016/S0040-6090(02)00699-5.

[16] M. Kassner, in: M. E. Kassner (Ed.), Fundamentals of Creep in Metals and Alloys, Elsevier, Amsterdam, second edition ed., 2008, pp. 9 – 93. URL: http://www.sciencedirect.com/science/article/pii/B9780080475615000026. doi:https://doi.org/10.1016/B978-0-08-047561-5.00002-6.

[17] F. H. Norton, The creep of steel at high temperatures, 35, McGraw-Hill Book Company, Incorporated, 1929.

[18] G. A. Slack, Journal of Applied Physics 35 (1964) 3460 – 3466. URL: https://doi.org/10.1063/1.1713251. doi:10.1063/1.1713251. arXiv:https://doi.org/10.1063/1.1713251.

[19] Plansee, Propertities of molybdeum, https://www.plansee.com/en/materials/molybdenum.html, ????

[20] R. R. Reeber, K. Wang, MRS Proceedings 622 (2000) T6.35.1. doi:10.1557/PROC-622-T6.35.1.

[21] J. Porter, W. Blumenthal, A. Evans, Acta Metallurgica 29 (1981) 1899 – 1906. URL: http://www.sciencedirect.com/science/article/pii/0001616081900274. doi:https://doi.org/10.1016/0001-6160(81)90027-4.

[22] J. F. Shackelford, W. Alexander, CRC Materials Science and Engineering Handbook, third edition ed., CRC press LLC, 2001.

[23] Kanthal, Propertities of apmt, https://www.kanthal.com/en/products/material-datasheets/tube/kanthal-apmt/, ????

[24] K. G. Field, M. A. Snead, Y. Yamamoto, K. A. Terrani, Handbook on the Material Properties of FeCrAl Alloys for Nuclear Power Production Applications (FY18 Version: Revision 1), Technical Report, 2018. doi:10.2172/1474581.

[25] P. Seiler, M. Bäker, J. Rösler, Computational Materials Science 80 (2013) 27 – 34. URL: http://www.sciencedirect.com/science/article/pii/S0927025613002000. doi:https://doi.org/10.1016/j.commatsci.2013.04.028, recent Advances in Computational Mechanics of Materials.

[26] Z. C. Jou, A. V. Virkar, Journal of the American Ceramic Society 73 (1990) 1928 – 1935. URL: https://ceramics.onlinelibrary.wiley.com/doi/abs/10.1111/j.1151-2916.1990.tb05247.x. doi:10.1111/j.1151-2916.1990.tb05247.x. arXiv:https://ceramics.onlinelibrary.wiley.com/doi/pdf/10.1111/j.1151-2916.1990.tb05247.x.

[27] D. R. Clarke, Current Opinion in Solid State and Materials Science 6 (2002) 237 – 244. URL: http://www.sciencedirect.com/science/article/pii/S1359028602000748. doi:https://doi.org/10.1016/S1359-0286(02)00074-8.

[28] F. N. Rhines, J. S. Wolf, Metallurgical Transactions 1 (1970) 1701 – 1710. URL: https://doi.org/10.1007/BF02642020. doi:10.1007/BF02642020.

[29] D. Clarke, Acta Materialia 51 (2003) 1393 – 1407. URL: http://www.sciencedirect.com/science/article/pii/S1359645402005323. doi:https://doi.org/10.1016/S1359-6454(02)00532-3.